Complex magnetic textures in Ni/Ir$_n$/Pt(111) ultrathin films

P. C. Carvalho,[1] I. P. Miranda,[1] A. B. Klautau,[2,*] A. Bergman,[3] and H. M. Petrilli[1]

[1] *Universidade de São Paulo, Instituto de Física, Rua do Matão, 1371, 05508-090 São Paulo, São Paulo, Brazil*
[2] *Faculdade de Física, Universidade Federal do Pará, CEP 66075-110, Belém, PA, Brazil*
[3] *Department of Physics and Astronomy, Uppsala University, 75120 Box 516 Sweden*

(Dated: May 26, 2021)

A combined approach using first-principles calculations and spin dynamics simulations is applied to study Ni/Ir$_n$/Pt(111) ($n = 0, 1, 2$) films. The lowest-energy states are predicted to be almost degenerate with negligble energy differences between pure spin-spiral and skyrmionic states. Moreover, for $n = 0$ and $n = 1$, we found that metastable skyrmioniums can occur, which are characterized by a slightly lower stability with respect to the external fields, enhanced lifetime, and the same critical current density as skyrmions. The spontaneous low temperature skyrmions, with ∼10 nm to ∼20 nm size, arise from a large Dzyaloshinskii–Moriya (DM) and Heisenberg exchange interactions ratio and, in particular, from a large in-plane DM vector component for nearest neighbors. The skyrmions become larger, faster and more dispersed with the enhancement of the Ir buffer thickness. Also, with increasing n, the skyrmions stability decrease when an external magnetic field is applied or the temperature is raised.

I. INTRODUCTION

Magnetic skyrmions are topologically protected chiral spins structures [1, 2] and, although the first experimental observation in MnSi bulk [3–5] is relatively recent, a vast research has already been made exploring the existence of these nanostructures in different materials. The search for faster magnetic storage devices and a larger storage capacity, among other features, has drawn attention to new magnetic nanostructures [1, 6, 7]. For instance, the presence of skyrmions has been reported in several metallic multilayers [8–13]. However, the exact conditions for the formation of skyrmions are not yet completely known.

The Dzyaloshinskii–Moriya (DM) [14, 15] as well as the Heisenberg exchange interactions [16] have shown to play an important role in the formation of skyrmions [17]. The DM is an anti-symmetric interaction which is non-zero in the presence of broken inversion symmetry. Its strength can be related to a high spin orbit coupling (SOC) [1] and it has been shown that it can also be associated with the degree of $3d$-$5d$ hybridization around the Fermi energy for certain materials [18]. Moreover, the formation of skyrmions has been explored in the literature regarding the DM interaction strength. For instance, C. Moreau-Luchaire et al. [11] experimentally observed room temperature skyrmions in Ir/Co/Pt asymmetric multilayers, stabilized by a large DM interaction. While the DM induces a chirality sense in the system, the Heisenberg interactions can favor a collinear (or non-collinear, through magnetic frustrations) alignment of spins, so the formation of skyrmions in magnetic films can be understood in terms of a competition between these interactions [19]. Therefore, interfaces composed by magnetic materials and high SOC elements are good candidates to search for skyrmions.

Among the systems composed by high SOC elements and magnetic materials, the study of Ni/Pt(111) and Ni/Ir(111) ultrathin films [18, 20] stands out, regarding its electronic structure, exchange and DM interactions. It has been shown that the DM interaction is smaller for ultrathin Ni layers than for systems with other $3d$ transition metals, such as Fe and Co. In Ref. [20], it was also revealed that, as the exchange and DM interactions were often of the same order of magnitude, there is a possibility of complex noncollinear configurations in the ground state of Ni clusters on Pt(111) and Ir(111) surfaces. However, to the best of our knowledge the magnetic properties of Ni/Ir$_n$/Pt(111) ultrathin films have not yet been studied.

Other magnetic structures that stand out in recent literature are magnetic skyrmioniums (or 2π-skyrmions) [21]. These are doughnut-like nontopological solitons, which have been proposed and studied theoretically [22, 23], as well as experimentally verified [21, 24]. They have been attracting much attention due to its $q = 0$ [25] topological charge. This characteristic makes these structures unaffected by the so-called skyrmion Hall effect (SkHE) [26], which, if present, forces the skyrmion to deviate from the current direction and may represent a challenge for future design of magnetic devices [27], specially for racetrack applications, as it can cause an annihilation of the skyrmion at the edges.

Here, we use atomistic spin dynamics simulations in combination with first principles calculations to predict the magnetic configurations of Ni/Ir$_n$/Pt(111) ultrathin films, with $n = 0$, 1 and 2. By using a density functional theory (DFT) based method, we calculate Heisenberg exchange and DM interactions. These quantities are used as input in atomistic spin dynamics simulations aiming to predict the Ni layers magnetic ground state. Skyrmions stabilities, regarding temperature and mag-

* aklautau@ufpa.br

netic fields, are investigated through the Ni/Ir$_n$/Pt(111) phase diagram. Furthermore, skyrmions and skyrmioniums shape, as well as their velocities under applied currents, are also analyzed.

II. COMPUTATIONAL METHODS

Electronic structure calculations were performed with the real-space linear-muffin-tin-orbital within the atomic sphere approximation (RS-LMTO-ASA) method [28–34] to obtain the magnetic ground state properties. The RS-LMTO-ASA has been proven to be suitable to describe complex magnetic systems [31–37]. To obtain the electronic density, the Haydock recursion [38] method with the Beer-Pettifor terminator [39] was used. Fully relativistic first principles calculations were performed with the local spin density approximation (LSDA) [40], for the exchange-correlation functional, and the recursion cut-off set to $LL = 22$. The exchange coupling (J_{ij}) and DM vector ($\vec{D}_{ij}$), between atomic sites i and j located at the surface, were calculated for a ferromagnetic configuration using the RS-LMTO-ASA code [16, 41, 42]. Since the J_{ij} and $|\vec{D}_{ij}|$ values can be different for (i, j) pairs of atoms in the same neighboring shell, due to the influence of the lower layer displacement that follows the fcc(111) stacking, the average was considered, for each interatomic distance.

We studied Ni/Ir$_n$/Pt(111), where $0 \leq n \leq 2$ is the number of Ir spacer layers. A cluster of $\sim 6,000$ atoms was built to simulate the fcc(111) ultrathin layer in real space with the experimental Pt(111) lattice parameter 3.92 Å. The system is composed by: one layer of atoms represented by empty spheres to mimic vacuum; one layer of Ni atoms (denoted as *s* layer) below the empty spheres; n layers of Ir atoms adjacent to the Ni layer, with $0 \leq n \leq 2$ (denoted as *s-1*, *s-2* and *s-3* layers); five layers of Pt atoms below the Ni layer (when $n = 0$) or the Ir layers (when $n \neq 0$).

The atomistic spin dynamics (ASD) simulations were performed with the UppASD code [43–45]. Firstly, the system is brought to its ground state through Monte Carlos (MC) simulations, from a temperature T larger than the Curie temperature T_C ($T > T_C$) to $T \sim 0$ K. In this initial phase, the atomic spin directions are varied in order to obtain the spin configuration with minimum energy. With the ground state configuration, the Landau-Lifshitz-Gilbert (LLG) equation [44, 46] is used to obtain the time evolution of each atomic spin and relax the system.

The connection between RS-LMTO-ASA and ASD simulations is made by the Hamiltonian

$$\mathrm{H} = -\sum_{i \neq j} J_{ij}(\hat{e}_i \cdot \hat{e}_j) - \sum_{i \neq j} \vec{D}_{ij} \cdot (\hat{e}_i \times \hat{e}_j) - \sum_i \vec{B}_{\mathrm{ext}} \cdot \hat{e}_i \quad (1)$$

where the Heisenberg exchange interaction (J_{ij}), Dzyaloshinskii–Moriya interaction ($\vec{D}_{ij}$) and the local magnetic moment ($\vec{m}_i = m\hat{e}_i$) are obtained from first principles calculations. The external magnetic field $\vec{B}_{\mathrm{ext}}$ can be included in the Hamiltonian optionally. Here, we found that a square lattice with 280×280 atomic spins is enough to simulate the Ni monolayer and used a realistic $\alpha = 0.05$ damping value, which has been shown to be suitable for similar surfaces [47–49]. We notice that only the Ni layer is simulated, since the influence of Ir and Pt atoms are included in the computation of the J_{ij} and $|\vec{D}_{ij}|$ interactions between Ni atoms. The skyrmions stabilities are analysed through the topological charges q (of each skyrmion) or $Q = \sum_i q_i$ (of the entire lattice).

III. RESULTS AND DISCUSSION

A. *Ab initio* calculations

Table I presents the local spin magnetic moment (m) of a representative atom at each layer in the Ni/Ir$_n$/Pt(111) systems studied here. The effect of the insertion of Ir spacer layers is to decrease the Ni local magnetic moment (m_{Ni}), up to $\Delta m_{\mathrm{Ni}} = 0.18\ \mu_B$. A similar reduction in m_{Ni} can also be found from Ni/Pt(111) to Ni/Ir(111), in the literature [20]. Furthermore, the induced magnetic moment at the *s-1* layers in Ni/Pt(111) and Ni/Ir$_1$/Pt(111) are equal, but are smaller in the Ni/Ir$_2$/Pt(111) case. The induced moments at the *s-1* layers can be explained by the hybridization of $3d$-$5d$ states (see Appendix A).

TABLE I: Local magnetic moment m (in μ_B/atom) of a typical atom in the first three layers of the Ni/Ir$_n$/Pt(111) systems. The layers are denoted by *s*, *s-1* and *s-2* (see text).

	$n = 0$		$n = 1$		$n = 2$	
s	Ni	0.60	Ni	0.52	Ni	0.42
s-1	Pt	0.12	Ir	0.12	Ir	0.06
s-2	Pt	0.03	Pt	0.01	Ir	-0.01

Heisenberg (J_{ij}) and strength of the DM ($|\vec{D}_{ij}|$) interactions between Ni atoms in the Ni/Ir$_n$/Pt(111) systems are shown in Fig. 1 as a function of the interatomic distance. Ni *bulk fcc* J_{ij}'s, calculated with the same method [50], are also presented. It can be seen that the successive addition of Ir spacer layers causes a significant decrease of the Ni-Ni nearest neighbors (NN) exchange coupling (J_1), following the same m_{Ni} trend: the largest J_1 is for Ni/Pt(111) ($n = 0$), by adding one Ir spacer layer ($n = 1$) it decreases almost 50% and for two Ir spacer layers ($n = 2$) the interaction is even smaller.

This trend (reduction of J_1 as the number of Ir spacer layers is increased) is in accordance with the comparative behavior of the extreme cases, Ni/Pt(111) and Ni/Ir(111), reported in the literature [20]. It can also be seen From Fig. 1(a) that J_{ij} decrease significantly for

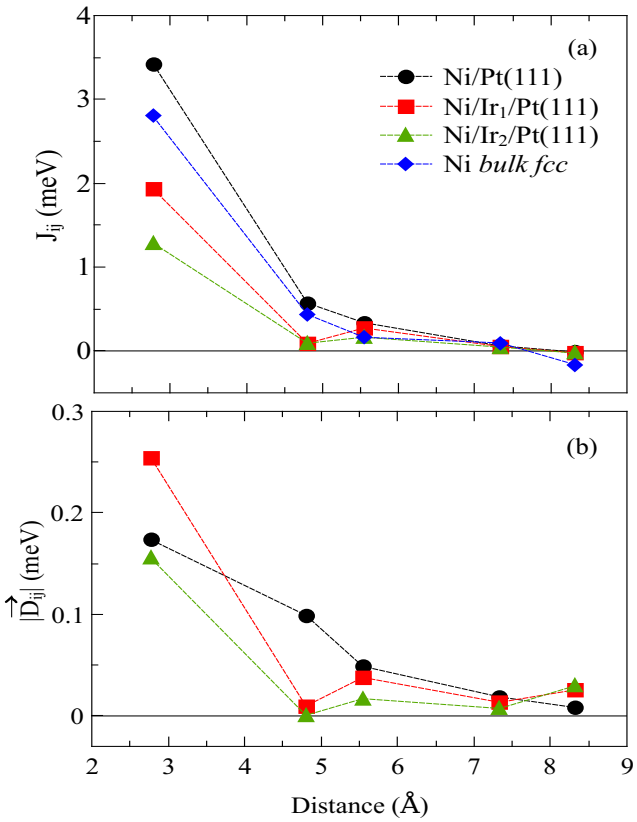

FIG. 1: Ni-Ni (a) Exchange coupling (J_{ij}) and (b) DM interaction strength ($|\vec{D}_{ij}|$) as a function of the interatomic distance for Ni/Ir$_n$/Pt(111) ($n = 0$, 1 and 2). Data for Ni *bulk fcc* obtained from Ref. [50]. The dotted lines are guides to the eyes. Convention symbols are the same for (a) and (b).

distances larger than 5 Å. Interestingly, J_1 is larger in Ni *bulk* than in the ultrathin layers with Ir spacers, but smaller than in Ni/Pt(111).

From Fig. 1(b) we observe that, analogous to the exchange coupling, the DM interaction strengh is larger for NN (D_1) and decreases for further neighbors, with a certain oscillation in the values. Remarkably is the NN interaction for $n = 1$ ($D_1 = 0.25$ meV) compared to $n = 0$ and $n = 2$. In order to understand this behaviour we note that three aspects have been suggested to contribute to the DM interaction: (a) the strength of SOC in a 5d substrate; (b) the inversion symmetry breaking; and (c) the spin polarization between 3d-5d interface atoms [18]. The presence of a larger DM interaction for $n = 1$, compared with $n = 0$, can then be explained by a higher symmetry breaking (more heterogeneous system), although Ir SOC is smaller than Pt, and the induced magnetic moments at the interfaces (*s-1* layer) have the same value (see Table I). The induced moment in the $n = 2$ case is smaller than for $n = 0$ and $n = 1$, the SOC is also smaller, and this inclusion of two Ir layers tends to the behaviour of the system in the extreme case of Ni/Ir(111). Also, from Fig. 1(b), we notice that, Ni/Ir$_1$/Pt(111) has the largest magnitude of DM interaction for NN, and for next-nearest-neighbours (NNN) the DM interaction is much stronger in Ni/Pt(111) compared to the other two systems. Therefore, only D_1 is relevant in the $n = 1$ and $n = 2$ cases.

Besides the strength of the DM vector, the direction is also an important aspect to be analyzed, since for a *fcc*(111) surface the DM direction is not completely determined from the Moriya's symmetry rules [15, 51]. The image of the hexagonal island with the DM vectors representing the interaction between Ni atoms, here obtained, are shown in Fig. 2. We verified that the DM vectors follow the rule $\vec{D}_{ij} \cdot \vec{R} = 0$ [15, 51], where $\vec{R}$ is the vector connecting the i and j sites. The rotational senses of the vectors are represented with black arrows. We see that adding Ir layers in Ni/Ir$_n$/Pt(111) does not change the rotational sense of the DM vectors. Moreover, the vectors are mostly in the plane of the surface, i.e. they have a small out-of-plane component. In Fig. 2(c), some arrows are not shown due to a very small DM strength.

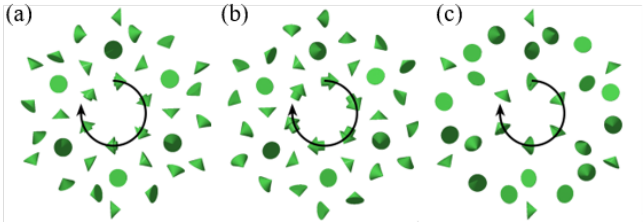

FIG. 2: $\vec{D}_{ij}$ between the central Ni and the Ni atom in the site of the arrow in: (a) Ni/Pt(111), (b) Ni/Ir$_1$/Pt(111) and (c) Ni/Ir$_2$/Pt(111). Arrow sizes are proportional to the vectors strengths. In (c), missing vectors are due to vanishing interaction strengths.

B. Spin dynamics

The extracted Heisenberg and DM interactions allow careful analyses of the magnetic order and finite temperature behaviours by means of atomistic spin dynamics. Firstly, we performed spin dynamics simulations for the Ni/Ir$_n$/Pt(111) systems, setting $B = 0$ and $T = 0$: the ground state configurations obtained were, almost degenerate, spin spirals and skyrmions (see Appendix C). The energy difference of these two magnetic configurations is of the order of a few μeV/atom, what is below the estimated numerical accuracy of the present DFT calculations. We have then chosen to study the states which presented skyrmions (as shown in Fig. 3), and considered the vector direction perpendicular to the ultrathin film as the z axis. The skyrmions observed here are Néel-type (topological charge $q = -1$) and for Ni/Pt(111) and Ni/Ir$_1$/Pt(111), we also noticed the presence of metastable skyrmioniums (see sub-section III D). The spin dynamics calculations were repeated several

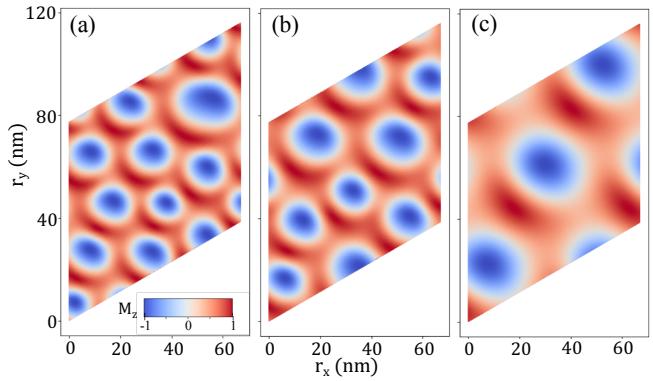

FIG. 3: Snapshot of a magnetic Ni layer configuration in: (a) Ni/Pt(111), (b) Ni/Ir$_1$/Pt(111) and (c) Ni/Ir$_2$/Pt(111), with $T = 0$ K and $B = 0$ T. The color represents the z-component of each spin (M_z).

times, such that skyrmions' diameters and densities could be estimated, as well as an uncertainty associated with each quantity. These values are in Table II. It can be

TABLE II: Diameter and density of skyrmions for Ni/Ir$_n$/Pt(111).

n	diameter (nm)	density (10^{-4} nm^{-2})
0	11.0 ± 2.8	9.0 ± 4.7
1	12.1 ± 3.4	7.0 ± 3.9
2	16.5 ± 6.6	4.5 ± 2.5

seen that skyrmions are nearly of the same size for $n = 0$ and 1, while the density decreases as the number of Ir layers increases. If the magnetic ground state would be a skyrmion crystal, all skyrmions would have the same size and a constant density. Thus, the fact that the skyrmions here occur with random variations in size and densities implies that these are, indeed, not the ground state solution. Instead, they occur as metastable states with very low activation energies. In the $n = 2$ case, skyrmions are slightly larger (around 30%) and the density is 64% smaller than in $n = 1$. This density decrease, when the second Ir layer is inserted, is too large to be explained by a diameter increase, what means that the skyrmions are more distant from each other, as can be seen in Fig. 3(c).

Further understanding of the physical mechanisms playing a role here can be achieved by analysing and comparing the behaviour of the Ni/Ir$_n$/Pt(111) with other 3d/Ir$_n$/Pt(111) systems. With this aim, we also performed calculations for Co/Ir$_n$/Pt(111), using the same methodology. Since this comparison is not the main focus of the present work, details for the Co based systems are shown in the Appendix B. The magnetic Co/Ir$_n$/Pt(111) ground state configurations are composed by domain walls, according to the present results and in agreement with Ref. [52]. This intriguingly different ground state magnetic configurations for Co- and Ni-based systems can be explained by analyzing the Heisenberg exchange and DM interaction behaviours. The Co-Co exchange interactions are strongly ferromagnetic and larger than the Ni-Ni, as could be expected. Nevertheless, the DM interaction in both, Co and Ni, systems are found to be of the same order of magnitude. Therefore, the ratio of the D_1 component parallel to the plane ($D_1^{\parallel}$) to J_1 is larger for Ni ultrathin layers compared to analogous Co-based systems (see Table VII in the Appendix B). In addition, the DM vectors present different behaviours in Co/Ir$_n$/Pt(111) and Ni/Ir$_n$/Pt(111). While the $\vec{D}_1^{\rm Ni}$ is mostly in the plane of the ultrathin film, $\vec{D}_1^{\rm Co}$ presents large out-of-plane components. Moreover, the sense of rotation of the Co-Co DM vectors changes as one includes Ir spacer layers (see Fig. 11 in Appendix B). Therefore, we infer that the origin of the complex noncollinear magnetic nanostructures in the ground state of Ni/Ir$_n$/Pt(111) are related to the fact that J_{ij} and $|\vec{D}_{ij}|$ have comparable magnitudes. Besides that, the presence of a significant $\vec{D}_1^{\rm Ni}$ component in the plane of the surface might also favour the formation of skyrmions in these systems.

C. Phase diagrams

We turn now our focus to the investigation of skyrmions stability with respect to temperature (T) and external magnetic field (B). In Fig. 4 and Table III, the phase diagrams and the corresponding ranges for the spin spiral (SS) and skyrmion lattice (SkL) phases, are respectively shown.

TABLE III: External magnetic field B (in T) and temperature T (in K) intervals where there are spin spirals (SS) or skyrmions lattice (SkL) phases in Ni/Ir$_n$/Pt(111).

SS phase		
$n = 0$	$0 \lesssim B \lesssim 0.4$	$0 \lesssim T \lesssim 50$
$n = 1$	$0 \lesssim B \lesssim 0.5$	$0 \lesssim T \lesssim 25$
$n = 2$	$0 \lesssim B \lesssim 0.1$	$0 \lesssim T \lesssim 40$
SkL phase		
$n = 0$	$0.4 \lesssim B \lesssim 2.1$	$0 \lesssim T \lesssim 100$
$n = 1$	$0.4 \lesssim B \lesssim 1$	$0 \lesssim T \lesssim 50$
$n = 2$	$0.1 \lesssim B \lesssim 0.4$	$0 \lesssim T \lesssim 40$

The external field, when applied, was oriented outwards from the ultrathin layers ([111] direction). We also calculated the critical temperatures ($T_{\rm crit}$) for each magnetic field value, where $T > T_{\rm crit}$ is the paramagnetic phase. Our results show that as n increases, the range which we find skyrmions (SkL phase) decreases, indicating that they are less stable with the increasing Ir buffer thickness. This is consistent to what was observed experimentally for the limiting case Ni/Ir(111) ($n \to \infty$), in which no magnetic contrast was found [53].

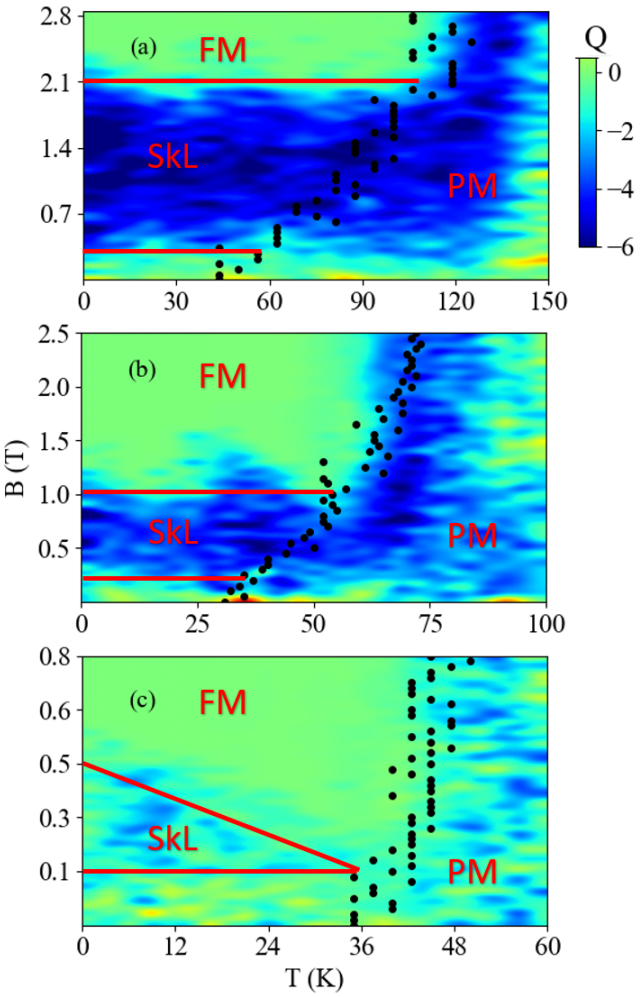

FIG. 4: Phase diagrams for (a) Ni/Pt(111), (b) Ni/Ir_1/Pt(111) and (c) Ni/Ir_2/Pt(111). Black dots are critical temperatures, T_{crit}, for each magnetic field. Colors code represent the topological charge of the lattice (Q). The ferromagnetic (FM), paramagnetic (PM) and skyrmion lattice (SkL) phases are indicared in red.

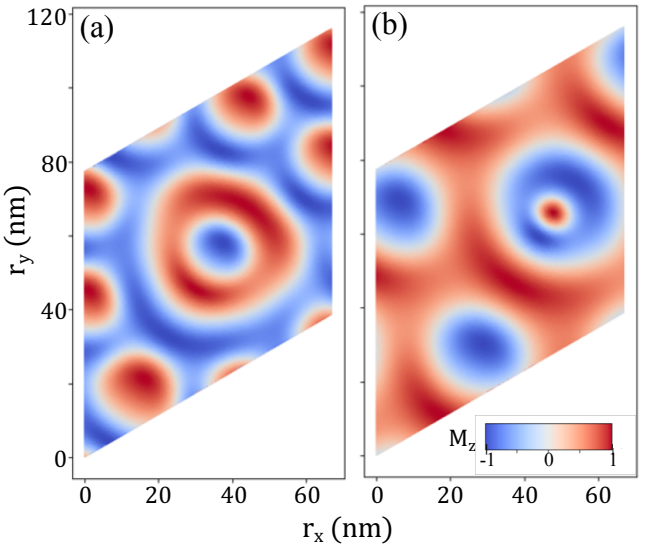

FIG. 5: Magnetic configuration, with $T = 10^{-4}$ K and $B = 0$ T, obtained with spin dynamics calculations for: (a) Ni/Pt(111) and (b) Ni/Ir_1/Pt(111). Examples of states with spontaneous skyrmioniums. The color represents the z-component of each spin (M_z).

D. Skyrmioniums

We found,for the Ni/Ir_n/Pt(111), spontaneous single skyrmioniums in the cases $n = 0$ and $n = 1$ with zero external magnetic field and low temperatures ($T = 10^{-4}$ K): examples of these states are shown in Fig. 5(a) and (b), respectively. The configurations presenting single skyrmioniums were found to be metastable with respect to the SS state (see Appendix D), and we expect that they can eventually appear in an experimental setup of Ni/Pt(111) and Ni/Ir/Pt(111).

We inspected the skyrmionium stability from two points of views: external magnetic field and temperature. In the first case, we verified that the skyrmionium vanishes with $B \sim 2.08$ T for $n = 0$ and $B \sim 0.9$ T for $n = 1$. These limits could be extracted from the evolution of the topological charge of the system with respect to B (see Fig. 15 in the Appendix D). The lower critical value of B for Ni/Ir_1/Pt(111) is expected, since from the phase diagrams the SkL is less stable than for Ni/Pt(111) (Table III). We note, however, that the critical field is slightly lower than the obtained for skyrmions in the phase diagrams. On the other hand, the influence of skyrmionium in the skyrmion lifetime (τ_{sk}) as a function of the temperature, as well as the skyrmion lifetime itself, are shown in Fig. 6. The calculation details are described in Appendix D. It is clear that the enhancement of the Ir buffer causes skyrmions to be more unstable from the temperature perspective. However, our results demonstrate that configurations containing skyrmioniums are more stable when compared to pure SkL, essentially due to the larger size of skyrmioniums and the consequent change in the entropy of the system [54].

E. Velocity and reading speed

In order to investigate the velocity of the skyrmions in the systems studied here, we followed the development of Iwasaki *et al.* [55], in which the current-velocity relation for skyrmions in the small damping limit is proportional to $\sqrt{j^2 - j_c^2}$ (j and j_c are the current density and critical current density, respectively). This also holds for skyrmioniums, due to their nature composed by two skyrmions with opposite topological charges ($q = \pm 1$). Knowing how skyrmions and skyrmioniums move is an issue of vital importance, as their motion via spin-transfer-torque (STT) is directly related to their control for potential applications in magnetic devices.

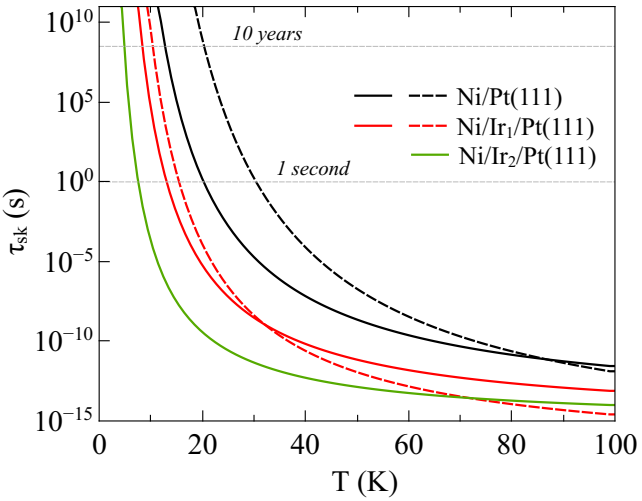

FIG. 6: Lifetime of skyrmions (full lines) and SkL + skyrmionium (dashed lines) configurations in Ni/Ir$_n$/Pt(111) as a function of temperature, considering B = 0 T, for configurations with skyrmioniums (Fig. 5).

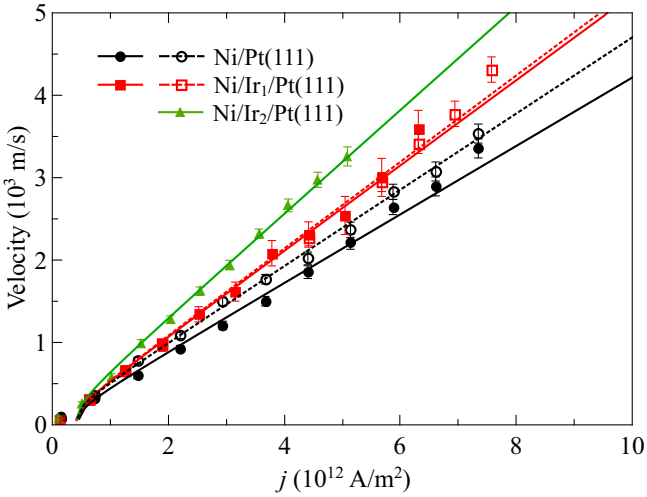

FIG. 7: Simulated skyrmion (solid points and lines) and skyrmionium (empty points and dashed lines) velocity for Ni/Ir$_n$/Pt(111) as a function of the applied current density (j) in the [1$\bar{1}$0] direction (in-plane). The lines represent the fit of a $v \propto \sqrt{j^2 - j_c^2}$ function, where the critical current density j_c is a constant (see Table IV).

Our results of skyrmions and skyrmionious motion in Ni/Ir$_n$/Pt(111) are shown in Fig. 7. From this figure it is straightforward to notice the linear dependence of the velocity (v) as a function of the current density (j). Furthermore, by inspection of the slopes, we notice that the inclusion of Ir layers between Ni and Pt makes the SkL movement faster. This can be related to the skyrmion density (Table II), which tends to decrease when the number of Ir spacer layers increases. Also, with larger diameters, skyrmions in Ni/Ir$_2$/Pt(111) experience a stronger deformation via STT that tends to enhance even more their velocity, which can be explained in terms of the Thiele equation approach [7, 25, 56, 57]. By fitting the obtained data, we can extract the critical current density (j_c) for each system, shown in Table IV.

As j_c do not depend on α, we find that the skyrmions in the Ni/Pt(111) ultrathin films are the latest to start moving, although all critical values are similar to each other. From the fitted curves we can also extract the current-driven mobility of SkL, defined as $\kappa = \frac{v}{j}$ [58, 59], where v is the velocity. The calculated κ values are also shown in Table IV, and corroborate with the observation of faster skyrmions and skyrmioniums when the Ir layers are present. We also note that skyrmionium driven mobility (and velocity) are slightly higher when compared to skyrmions in the same substrate, which agrees with previous findings for different systems [7, 25, 60]. It is related to the larger size of skyrmioniums and a consequently stronger deformation [7].

A crucial property of skyrmions for future applications in magnetic devices is the reading speed, i.e., how much information per unit of time can be read in that material. This quantity depends on several factors, including the magnetic damping. There are at least two ways to calculate the reading speed in a 2D material: (i) per area;

TABLE IV: Critical current density (j_c) and current-driven mobility (κ) for skyrmions and skyrmioniums in Ni/Ir$_n$/Pt(111).

Skyrmions		
n	j_c (10^{11} A·m^{-2})	κ (ms^{-1}/TA·m^{-2})
0	4.6 ± 1.3	427 ± 9
1	4.2 ± 0.4	533 ± 9
2	4.2 ± 0.3	651 ± 11
Skyrmioniums		
n	j_c (10^{11} A·m^{-2})	κ (ms^{-1}/TA·m^{-2})
0	4.4 ± 0.8	474 ± 8
1	4.2 ± 0.5	543 ± 9

and (ii) considering a single racetrack memory [1, 61], for which we presume a linear reading speed. In the case (i), assuming the simplest model of a reading square area A, the reading speed (R_s) can be approximated, in bits/s, as

$$R_s = v\rho\sqrt{A} = j\kappa\rho\sqrt{A}, \tag{2}$$

where ρ is the skyrmion density (Table II), and considering that each skyrmion represents a bit of information. Considering the values obtained for a current density $j = 1$ TA·m^{-2}, we get the reading speeds shown on Table V. On the other hand, for a single racetrack memory case and assuming that the linear skyrmion density, ρ_L, goes as $\rho_L \sim \sqrt{\rho}$, we can calculate the linear reading speed, R_{s_L}, as

$$R_{s_L} = v\rho_L, \tag{3}$$

for which we get the R_{s_L} values also shown in Table V. Therefore, by reducing the 2D skyrmion density, the enhancement of the Ir buffer in Ni/Ir_2/Pt(111) diminishes the average R_s, while it remains similar to the $n = 0$ and $n = 1$ cases, because of its enhanced skyrmion velocity. As R_s and R_{s_L} quantities depend on the density ρ (ρ_L), and we obtained only metastable single skyrmioniums, we can not ascribe them for this type of structure.

TABLE V: Ni/Ir_n/Pt(111) reading speeds: per area (R_s) and linear (R_{s_L}). The current density is $j = 1$ TA·m^{-2}.

n	R_s (Pb · s^{-1} · cm^{-2})	R_{s_L} (Gb · s^{-1})
0	3.8 ± 2.0	12.8 ± 3.4
1	3.7 ± 2.1	14.1 ± 3.9
2	2.9 ± 1.6	13.8 ± 3.8

For high current densities in both Ni/Pt(111) and Ni/Ir_1/Pt(111), we obtained an unzipping process of skyrmioniums [25, 62]. This large j enhances the transverse opposite driving spin Hall forces ($\vec{F}_{sh}$) from SkHE in the inner and outer skyrmions in a way that unbalances the confinement provided by the skyrmionium ring [17], compelling the structure to suffer a massive distortion and a consequent annihilation. In these conditions, the skyrmionium is transformed into to two separate spin textures with $q = \pm 1$. This skyrmionium annihilation is shown in Fig. 8, considering the Ni/Pt(111) system and $j \sim 1.5 \times 10^{13}$ A/m^2, between the time instants of $\tau_1 = 8.4$ ps and $\tau_2 = 13.2$ ps from the beginning of the simulation (time interval $\Delta\tau = 4.8$ ps). However, for lower current densities, the transverse forces are weak enough to be cancelled by the skyrmionium ring confinement (which impels an opposite force), and the structure is maintained along the track.

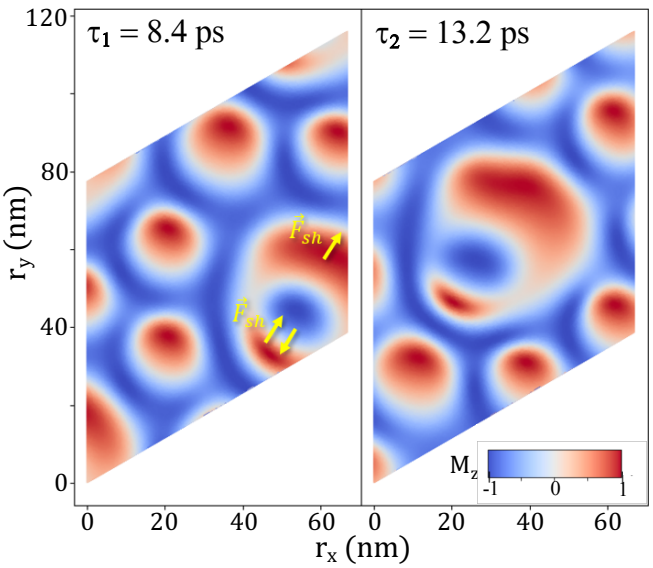

FIG. 8: Unzipping of a spontaneous skyrmionium (with $T = 10^{-4}$ K and $B = 0$ T) in Ni/Pt(111) for a high current density of $j \sim 1.5 \times 10^{13}$ A/m^2 in the $[1\bar{1}0]$ direction. Calculated time interval of $\Delta\tau = 4.8$ ps. $\vec{F}_{sh}$ is the spin Hall force.

IV. CONCLUSIONS

Local magnetic properties and the lower-energy state configurations of Ni/Ir_n/Pt(111) films (with $n = 0, 1, 2$) have been here obtained using first principles calculations and spin dynamics. The minimum energy state is found degenerated between spin spirals and a ferromagnetic skyrmion lattice. The presence of spontaneous skyrmions in Ni/Ir_n/Pt(111) points to a different behaviour, when compared to other similar metallic ultrathin layers. We infer that this is related to the fact that the D_1 to J_1 ratio is larger compared to Co/Ir_n/Pt(111), and that no significant out-of-plane DM vector component was obtained for the Ni-based systems. The skyrmions found here are small (10 nm $< d <$ 20 nm), but with the enhancement of the Ir buffer thickness they become: larger, more dispersed, faster and less stable (also in the presence of external magnetic fields and increasing temperature), and their lifetimes decays. The average linear reading speed is almost the same in all Ni/Ir_n/Pt(111) systems, while the reading speed per unit area decreases for $n = 2$ due to its diminished skyrmion density. For $n = 0$ and $n = 1$ metastable skyrmioniums were also found, which present the same critical current density as skyrmions and a slightly lower stability with respect to the external magnetic field. Due to their larger size, this can enhance the lifetime of the magnetic configuration when compared to a clean SkL and have shown to be somewhat faster than skyrmions. Therefore, this research not only contributes to the fundamental understanding of skyrmions and skyrmioniums in ultrathin films, but also opens a route towards the control of their properties via buffer thickness.

V. ACKNOWLEDGMENTS

H.M.P. and A.B.K. acknowledge financial support from CAPES, CNPq and FAPESP, Brazil. A.B. acknowledges eSSENCE. I.M. acknowledges financial support from CAPES, Finance Code 001, process n° 88882.332894/2018-01, and in the Institutional Program of Overseas Sandwich Doctorate, process n° 88881.187258/2018-01. P.C.C. acknowledges financial support from FAPESP, process 2020/05609-7. The calculations were performed at the computational facilities of the HPC-USP/CENAPAD-UNICAMP (Brazil), at the National Laboratory for Scientific Computing (LNCC/MCTI, Brazil), and at the Swedish National Infrastructure for Computing (SNIC).

Appendix A: Ni/Ir$_n$/Pt(111) electronic structure

The Local Density of States (LDOS) projected on a typical atom in the *s*, *s-1* and *s-2* layers, for the Ni/Ir$_n$/Pt(111) systems studied here, are shown in Fig. 9, where a charge transfer between $3d$ (Ni) and $5d$ (Ir or Pt) orbitals can be observed. After adding one Ir layer ($n = 1$), the Ni electronic structure is changed and $3d$ electrons, from both majority and minority bands, are transferred to Ir $5d$ orbitals, leading to a decrease in the $m_{\rm Ni}$ and inducing a non-null magnetic moment in the *s-1* layer. The induced magnetic moments in the Ni/Pt(111) and Ni/Ir$_1$/Pt(111) *s-1* layers are the same, indicating that the Ir and Pt layers exhibit analogous behaviours. For $n = 2$, the charge transfer is still responsible for the $m_{\rm Ni}$ reduction, but the Ir electronic structure is changed (in both layers *s-1* and *s-2*) and its the majority and minority bands are almost symmetric. Therefore, the addition of two Ir layers ($n = 2$) causes the induced magnetic moment in the *s-1* layer to decrease about 50% with respect to $n = 0$. We notice that, since the *s* and *p* LDOS are relatively symmetric in all cases, we limit our analysis to the *d* electrons.

Appendix B: Co/Ir$_n$/Pt(111) ultrathin films

Using the RS-LMTO-ASA code, and an analogous procedure (same cluster size and lattice parameters as described for Ni/Ir$_n$/Pt(111)) but replacing Ni by Co at the *s* layer, we investigated Co/Ir$_n$/Pt(111) ultrathin films with $n = 0$, 1 and 2.

As shown in Table VI the Co local magnetic moment ($m_{\rm Co}$) is not very sensitive to the Ir spacer thickness but the induced magnetic moment in the *s-1* layers decreases with increasing n.

TABLE VI: Local magnetic moment m (in μ_B/atom) of a typical atom in the first three layers of the Co/Ir$_n$/Pt(111) systems. The layers are denoted by *s*, *s-1* and *s-2* (see text).

	$n = 0$		$n = 1$		$n = 2$	
s	Co	1.80	Co	1.85	Co	1.82
s-1	Pt	0.31	Ir	0.28	Ir	0.19
s-2	Pt	0.14	Pt	0.05	Ir	-0.04

Heisenberg exchange and DM interactions for Co/Ir$_n$/Pt(111) are presented in Fig. 10; also shown J_{ij} data for Co *bulk fcc* from Ref. [50] (obtained with the same method). It can be noticed that all $J_1^{\rm Co}$ are similar (differing by $\sim 6\%$) and larger than in the Ni/Ir$_n$/Pt(111) cases (Fig. 1), what indicate a strong ferromagnetic coupling and a different behavior. The presence of Ir spacer layers change the strength of the DM interaction since the largest $D_1^{\rm Co}$ is for $n = 0$ and decreases for larger n. This can be explained by the smaller induced moment at the adjacent Ir layer

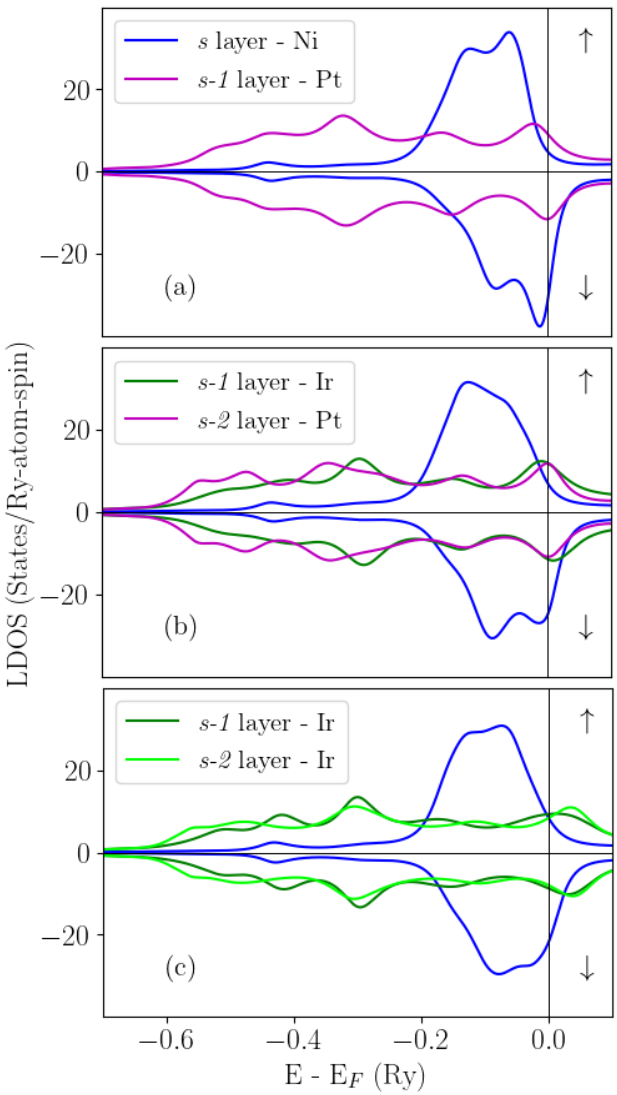

FIG. 9: Spin polarized LDOS at a typical atom in different layers (*s*, *s-1* or *s-2*) in (a) Ni/Pt(111); (b) Ni/Ir$_1$/Pt(111) and (c) Ni/Ir$_2$/Pt(111). Color conventions are: Ni (blue), Pt (pink) and Ir (light and dark green).

compared with the Pt one (see Table VI).

The J_{ij} for Co/Pt(111) from Ref. [63] (obtained using the Korringa-Kohn-Rostoker method), agree well to the present results. The small difference found in the case of J_1 was also reported in Ref. [20] ($\sim 7\%$) comparing Co/Pt(111) and Co/Ir(111). We notice that the Co/Ir$_n$/Pt(111) J_{ij} and $\vec{D}_{ij}$ behaviors slightly differ from Ref. [52] what may be related to structural relaxations as well as different methodologies to calculate J_{ij} and $\vec{D}_{ij}$.

Contrasting to the Ni systems (Fig. 2), the DM vector directions in Co/Ir$_n$/Pt(111), shown in Fig. 11, exhibit a change in the rotational sense, with the presence of the Ir spacer layer. Moreover, the $\vec{D}_{ij}^{\rm Co}$ and $\vec{D}_{ij}^{\rm Ni}$ in-plane and out-of-plane components behave differently. In order to inspect that, in Fig. 12, the out-of-plane components

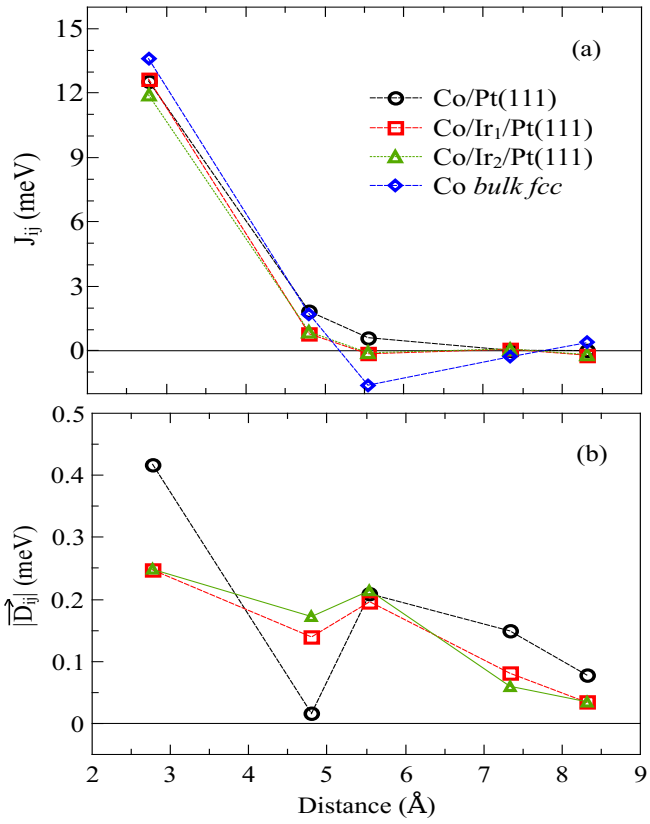

FIG. 10: Co-Co (a) Heisenberg exchange coupling (J_{ij}) and (b) DM interaction strength ($|\vec{D}_{ij}|$) as a function of the interatomic distance in Co/Ir$_n$/Pt(111) for n = 0, 1 e 2. Data for Co *bulk fcc* obtained from Ref. [50]. The dotted lines are guides to the eyes.

of the DM vectors ($D_{ij}^{\perp}$) as a function of the distance between two Co or Ni atoms are shown. While $\vec{D}_{ij}^{\rm Co}$ present a large out-of-plane component, the $\vec{D}_{ij}^{\rm Ni}$ vectors are mainly in the plane, as presented in sub-section III A.

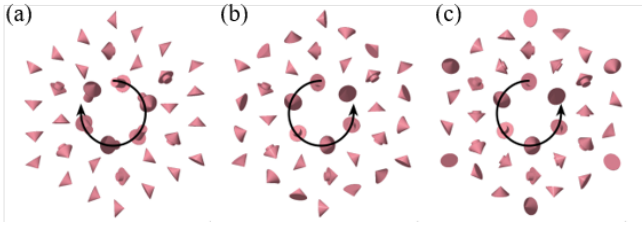

FIG. 11: $\vec{D}_{ij}$ between the central Co and the Co atom in the site of the arrow in: (a) Co/Pt(111), (b) Co/Ir$_1$/Pt(111) and (c) Co/Ir$_2$/Pt(111). Arrow sizes are proportional to the vectors strengths.

In order to inspect the Heisenberg and DM behaviours, which differ from Co to Ni based systems, we calculate the $D_1^{\parallel}/J_1$ ratio, where $D_1^{\parallel}$ is the D_1 component parallel to the plane. The results are shown in Table VII.

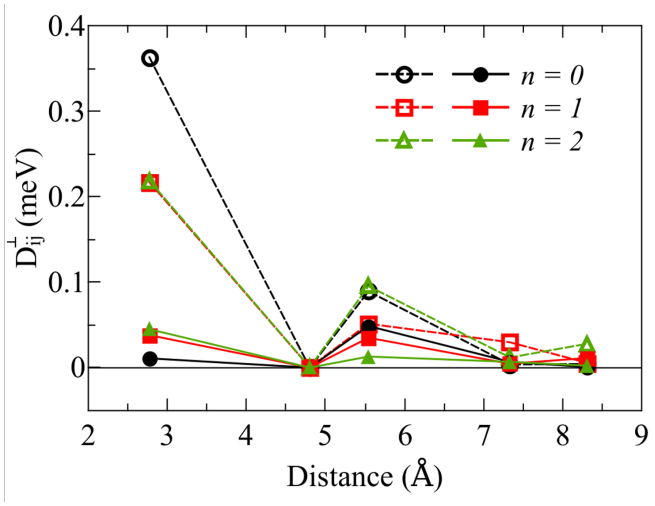

FIG. 12: Out-of-plane components of the DM vector ($D_{ij}^{\perp}$) for: Co/Ir$_n$/Pt(111) (dashed lines, open symbols) and Ni/Ir$_n$/Pt(111) (solid lines, full symbols).

We infer that the existence of skyrmions as ground-state in Ni/Ir$_n$/Pt(111), in contrast to a spin-spiral ground-state in Co/Ir$_n$/Pt(111), is related to the fact that Co ultrathin layers exhibit smaller $D_1^{\parallel}/J_1$ ratios, for each n, when compared to the Ni-based systems. Atomistic spin-dynamics calculations for Co/Ir$_n$/Pt(111) were here performed, resulting, in agreement with Ref. [52], in a spin-spiral ground-state. Nevertheless, since the chirality is introduced when the DM term in the spin Hamiltonian drives a spin rotation to be energetically favorable, we calculated the energy contribution from the Heisenberg and DM interactions in Ni/Ir$_n$/Pt(111) ultrathin layers. Here, we define the DM and Heisenberg total energies with respect to a typical site "0" ($D_0^{\rm total}$ and $J_0^{\rm total}$, respectively) by

$$D_0^{\rm total} = \sum_j \vec{D}_{0j} \cdot (\hat{e}_0 \times \hat{e}_j) \qquad \text{(B1)}$$

$$J_0^{\rm total} = \sum_j J_{0j} (\hat{e}_0 \cdot \hat{e}_j) \qquad \text{(B2)}$$

,

where the direction of the magnetic moments ($\hat{e}_0$ and $\hat{e}_j$) are obtained from spin dynamics simulations. The number of neighbors considered here was 36 (or 5 non-equivalent neighboring shells). The ratio $D_0^{\rm total}/J_0^{\rm total}$ for Ni/Ir$_n$/Pt(111) is also presented in Table VII. It has been shown in the literature that a larger D/J ratio favours a faster rotation of the spins, and drives a reduction of the skyrmion size [1, 57, 64]. Our results confirm that, indeed, larger $D_0^{\rm total}/J_0^{\rm total}$ ratios are related to more stable and smaller skyrmions, since the value in Ni/Pt(111) decreases (up to 90%) with increasing Ir buffer thickness.

TABLE VII: DM/Exchange ratios $D_1^{\parallel}/J_1$ (see text) and $D_0^{\text{total}}/J_0^{\text{total}}$ (Eq. (B1) and Eq. (B2)), for the Co and Ni systems studied here. All ratios are displayed in units $\times 10^{-3}$.

	Co/Ir$_n$/Pt(111)	**Ni/Ir$_n$/Pt(111)**	
n	$D_1^{\parallel}/J_1$	$D_1^{\parallel}/J_1$	$D_0^{\text{total}}/J_0^{\text{total}}$
0	16	50	4.2
1	9	130	2.9
2	9	115	0.4

Appendix C: Ni/Ir$_n$/Pt(111) magnetic ground state configuration

Ni/Ir$_n$/Pt(111) magnetic ground states were determined by performing calculations using the UppASD code and comparing the spin spirals (SS) and skyrmion lattices (SkL) energies. A spin spiral can be described by a wave vector $\mathbf{q}$, through the following equation

$$\hat{e}(\mathbf{r},\mathbf{q}) = \hat{s}\cos(\mathbf{r}\cdot\mathbf{q}) + \hat{n}\sin(\mathbf{r}\cdot\mathbf{q}) \qquad \text{(C1)}$$

where $\hat{e}$ is the local magnetization direction, $\mathbf{r}$ is the spin position and $\hat{s}$ and $\hat{n}$ are unit vectors defining the rotational plane of the spiral. Given the two unit vectors, we can map out the energy landscape by calculating the total energies of all spin spirals which have $\mathbf{q}$-vectors commensurate with the dimensions of the system. The spin spiral state with the $\mathbf{q}$-vector corresponding to the lowest energy was then identified and relaxed further, using overdamped zero-temperature spin dynamics simulations to let the system relax as far as possible. Skyrmion lattices were simulated using the same approach but then 3$\mathbf{q}$ spin spirals, i.e. a magnetic texture described by 3 $\mathbf{q}$-vectors with the same magnitude of $\mathbf{q}$ but rotated 120° between them, were considered. Furthermore, theses results were compared with the Monte Carlo (MC) simulations used to build the phase diagram. Here, the influence of the lattice on the results was analyzed as well. Thus, the procedure described above was done for the proposed ultrathin films, considering a square lattice size ($N \times N$), with $200 \leq N \leq 500$ for $n = 0$, 1, 2. We also considered two types of 1$\mathbf{q}$ simulations: spin spirals in the $\hat{x}$ direction (1$\mathbf{q}$ yz) and $\hat{y}$ direction (1$\mathbf{q}$ xz).

The results for both 1$\mathbf{q}$ and 3$\mathbf{q}$ calculations for the Ni ultrathin films are shown in Fig. 13. Notice that the energy vertical scale is in μeV, what implies that the curves are almost degenerate in the whole lattice size range studied here. Therefore, a typical lattice size of $N = 280$ was chosen and, in this case, for $n = 0$ and 1, the state with the minimum energy is a spin spiral in the $\hat{x}$ direction (1$\mathbf{q}$ yz), while for $n = 2$ the lower-energy state found is a spin spiral in the $\hat{y}$ direction (1$\mathbf{q}$ xz). However, the energy difference between these configurations and skyrmions (3$\mathbf{q}$) is, indeed, very low, indicating an almost degenerate SS and SkL state. Considering $N = 280$, our calculations show $\Delta E = 0.97$ μeV for $n = 0$, $\Delta E = 0.96$ μeV for $n = 1$, and $\Delta E = 0.76$ μeV for $n = 2$, always favouring the SS phase. Furthermore, we notice that the hierarchy of the considered states, i.e. the stability order (total energy competition) clearly depends on the system size. This points to the necessity of always performing a careful finite size scaling analysis, when discussing the stability of complex magnetic states.

As a result of the degeneracy obtained in the ground state, we can predict that spontaneous skyrmions shall be experimentally observed in these systems. We also note that, for $n = 2$, the SkL range is less homogeneous than for $n = 0$ and 1, intercalating the phase region with spin spiral state (see phase diagram in Fig. 4(c)). This can be understood in terms of the small ΔE found (Fig. 13), and less stable SkL under (B, T) ranges (Fig. 4 and Table III). More broadly, the stability of the skyrmions is diminished when the number of Ir layers increases in Ni/Ir$_n$/Pt(111). This can be directly related to the decrease (Fig. 1(a)) on the J_{ij} parameters.

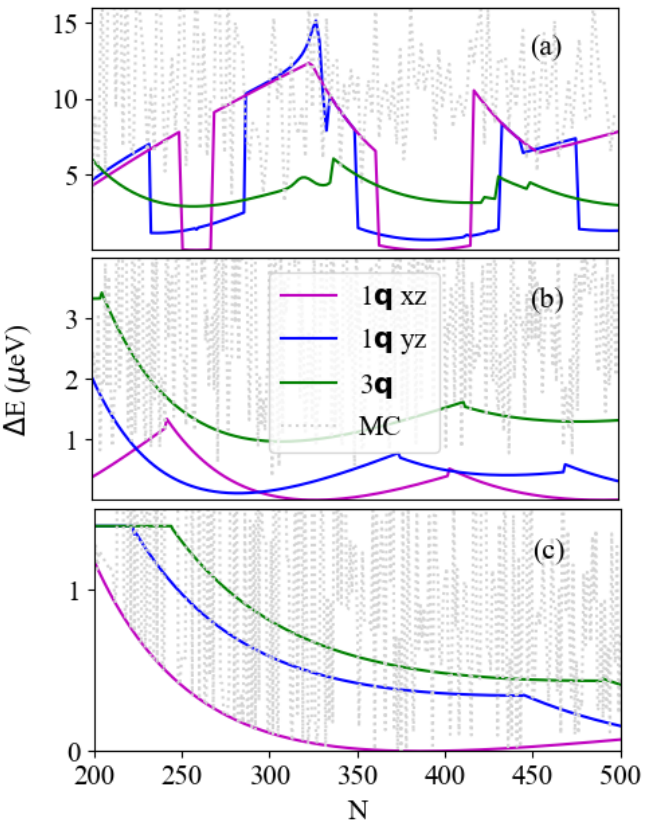

FIG. 13: Energy difference as a function of the lattice size N. Results for spins spirals (1$\mathbf{q}$), skyrmions (3$\mathbf{q}$) and Monte Carlo (MC) calculations performed for: (a) Ni/Pt(111); (b) Ni/Ir$_1$/Pt(111) and (c) Ni/Ir$_2$/Pt(111). The zero value is the minimal energy. Colour conventions are the same in all cases.

Appendix D: Skyrmioniums stability

Since skyrmioniums are characterized by a topological charge $q = 0$ (due to its doughnut-like structure composed by a skyrmion with $q = +1$ inside a skyrmion with $q = -1$, or vice-versa [25]) they are undetectable through q charge measurements, as other non-topological spin textures (ferromagnetic and antiferromagnetic mediums, or spin-spirals). However, our calculations have shown that these structures can emerge together with skyrmions in Ni/Pt(111) and Ni/Ir_1/Pt(111) as metastable states, with an energy difference with respect to the SS state of $\Delta E = 1.78\ \mu$eV ($n = 0$), and $\Delta E = 3.27\ \mu$eV ($n = 1$).

Spin dynamics simulations reveal that the annihilation of skyrmioniums in these systems with the action of external magnetic fields B occur by transforming them into regular skyrmions, what implies a topological $q = 0 \rightarrow q = \pm 1$ transition. Fig. 14 exhibits an example of this transition for a skyrmionium in Ni/Pt(111), from $B = 2.0$ T to $B = 2.1$ T (and $T = 10^{-4}$ K). Since we

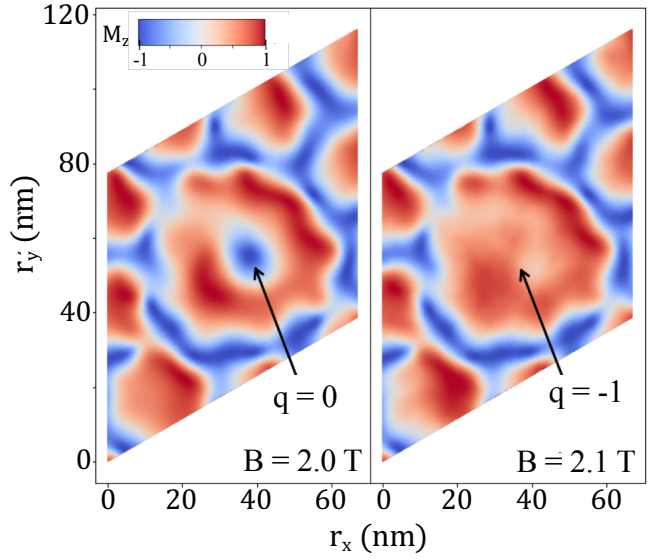

FIG. 14: Skyrmionium annihilation process with the action of an external magnetic field from $B = 2.0$ T to $B = 2.1$ T in Ni/Pt(111), resulting in a topological $q = 0 \rightarrow q = -1$ transition. Results for the low temperature regime of $T = 10^{-4}$ K.

obtain the topological charge Q of the whole spin system, the stability of the skyrmionium with respect to B can be inferred from a $Q - B$ diagram, together with the visual inspection of the resulting spin state, for each analyzed magnetic field. We note that the skyrmionium annihilation events are instantaneous, analogously to what was obtained for regular skyrmions [65]. We also remark that this field-stability of skyrmioniums should not depend on the damping α, as it is intrinsically related to the interactions in the spin model. The obtained $Q - B$ diagrams for Ni/Ir_n/Pt(111) (for $n = 0$ and $n = 1$) are shown in Fig. 15.

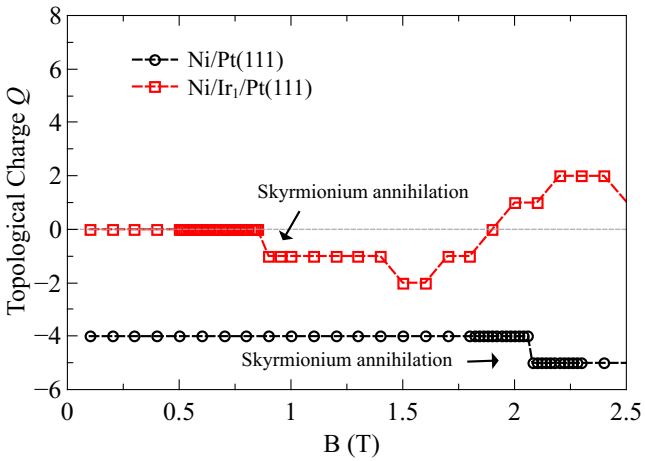

FIG. 15: $Q - B$ diagrams for: (black) Ni/Pt(111) and (red) Ni/Ir_1/Pt(111). The arrows indicate the magnetic field (B) magnitude in which the skyrmioniums are annihilated in each system. Results are for the low temperature regime of $T = 10^{-4}$ K. The lines are guides to the eyes.

From these results, we can determine the critical fields $B_{crit} \sim 2.08$ T for Ni/Pt(111) and $B_{crit} \sim 0.9$ T for Ni/Ir_1/Pt(111). As a consequence of these particular spin configurations, in which skyrmioniums can generate $q \neq 0$ structures, the topological charge fluctuates around $Q = 0$, resulting in skyrmions even in a higher range of magnetic fields than the described in Table III.

We also investigated the influence of skyrmionium in skyrmion lifetime as a function of the temperature, and compared the results with the lifetime of the pristine skyrmion lattice (τ_{sk}) in the same substrate. For this case, we considered $B = 0$ in all studied configurations. According to previous works [54, 65–68], it is known that the skyrmion creation is a nucleation process, and the lifetime should follows the Arrhenius law

$$\tau_{sk} \sim \tau_0 e^{\frac{\Delta E}{k_B T}}, \tag{D1}$$

being k_B and τ_0, respectively, the Boltzmann constant and a proportionality constant (the so-called attempt time), and ΔE the collapse energy barrier. Therefore, it is expected that for skyrmioniums this also holds. As we calculate the skyrmion number of the whole spin system (Q_{total}), the lifetime can be extracted from the $Q(t)$ function considering that the increase in Q_{total} is only due to the annihilation of downwards pointing skyrmions or the creation of a central-downwards pointing skyrmioniums (see Fig. 14, inverse process), the latter in the case of a system containing skyrmioniums. This means that the presence of upwards pointing skyrmions or antiskyrmions is excluded. In the stationary case (in which $\frac{dQ}{dt} = 0$), the skyrmion lifetime is obtained by multiplying the average time between skyrmion annihilation events with the average topological charge, $\bar{Q}_{total}$, analogously to what was done in Ref. [65]. With this definition, we calcu-

lated $Q(t)$ in a time interval of 25 ps, considering the Ni/Ir$_n$/Pt(111) SkL, and, in the case of $n = 0$ and $n = 1$, also the SkL with a skyrmionium configuration. An example of skyrmion lifetime as a function of temperature is shown in Fig. 16, for the Ni/Pt(111). By fitting Eq. (D1) in the τ_{sk} data, we obtain the collapse energy barriers and attempt times shown in Table VIII, which can be compared to the energy coming from the largest contributions of isotropic exchange interactions, from first to third neighbours (in the number of six each). Skyrmions are unwound if the central spin is rotated to the direction of the most external spin, and the strongest contributions for the stabilization of this central spin come from the nearest exchange interactions. Therefore, with ΔE and τ_0 obtained, then $\tau_{sk}(t)$ is determined (see Fig. 6 in the main text). The calculated collapse barriers decrease with larger thickness of the Ir buffer.

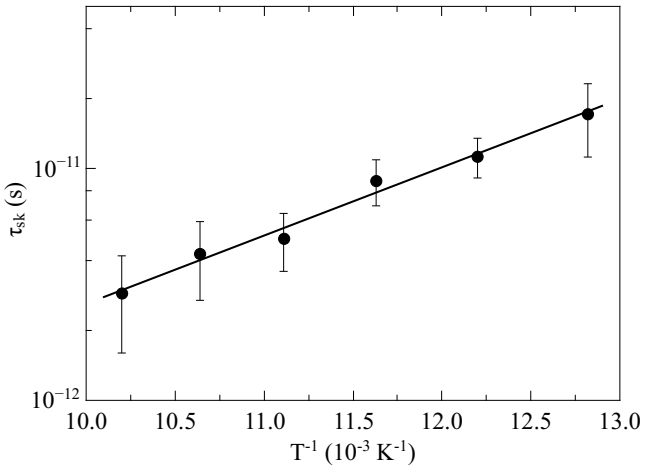

FIG. 16: Skyrmion lifetime τ_{sk} as a function of the inverse of the temperature T^{-1} for Ni/Pt(111), considering no external magnetic field ($B = 0$) and $\alpha = 0.05$. Arrhenius law (Eq. (D1)) fit (black line).

Similarly, we can consider the metastable configurations containing skyrmioniums for $n = 0$ and $n = 1$, shown in Fig. 5. The same analysis is performed as in the pure SkL case, but now with the influence of these $q = 0$ structures. The calculated ΔE and τ_0 values are also shonw in Table VIII. We notice an enhancement of the collapse energy barriers in both surfaces, what is consistent with von Malottki *et al.* [54] findings for Pd/Fe bilayers on Ir(111) and on Rh(111), where ΔE enhances with the skyrmion size. The Skyrmioniums radius are larger than in skyrmions, and contributes to the enhancement of ΔE in the entire magnetic configuration. This increase in ΔE diminishes the attempt time τ_0 by the compensation effect, related to entropy, reported by Wild *et al.* [68] for the B20 $Fe_{0.5}Co_{0.5}Si$ bulk. In all calculations we considered $\alpha = 0.05$, which could affect τ_0 [69], but not ΔE.

TABLE VIII: Skyrmion collapse energy barrier ΔE, sum of the exchange interactions up to third neighbours, and attempt time τ_0 (10^{-18}s), for Ni/Ir$_n$/Pt(111) skyrmion lattices obtained via fitting of the Arrhenius law (Eq. (D1)), with $\alpha = 0.05$ and $B = 0$. Corresponding values in parenthesis are obtained for the skyrmionium configurations.

n	$\frac{\Delta E}{k_B}$ (K)	$\frac{6}{k_B}(J_1 + J_2 + J_3)$ (K)	τ_0 (as)
0	678 (1202)	604	$\sim 3 \times 10^3$ (~ 7)
1	455 (616)	320	$\sim 8 \times 10^2$ (~ 5)
2	264	215	$\sim 7 \times 10^2$

[1] A. Fert, V. Cros, and J. Sampaio, Nat. Nanotechnol. **8**, 152 (2013).
[2] W. Jiang, G. Chen, K. Liu, J. Zang, S. G. t. Velthuis, and A. Hoffmann, Physics Reports **704**, 1 (2017).
[3] A. Neubauer, C. Pfleiderer, B. Binz, A. Rosch, R. Ritz, P. G. Niklowitz, and P. Böni, Phys. Rev. Lett. **102**, 186602 (2009).
[4] C. Pappas, E. Lelièvre-Berna, P. Falus, P. M. Bentley, E. Moskvin, S. Grigoriev, P. Fouquet, and B. Farago, Phys. Rev. Lett. **102**, 197202 (2009).
[5] S. Mühlbauer, B. Binz, F. Jonietz, C. Pfleiderer, A. Rosch, A. Neubauer, R. Georgii, and P. Böni, Science **323**, 915 (2009).
[6] X. Zhang, G. P. Zhao, H. Fangohr, J. P. Liu, W. X. Xia, J. Xia, and F. J. Morvan, Sci. Rep. **5**, 7643 (2015).
[7] B. Göbel, A. F. Schäffer, J. Berakdar, I. Mertig, and S. S. Parkin, Sci. Rep. **9**, 1 (2019).
[8] N. Romming, C. Hanneken, M. Menzel, J. E. Bickel, B. Wolter, K. von Bergmann, A. Kubetzka, and R. Wiesendanger, Science **341**, 636 (2013).
[9] M. Hervé, B. Dupé, R. Lopes, M. Böttcher, M. D. Martins, T. Balashov, L. Gerhard, J. Sinova, and W. Wulfhekel, Nat. Commun. **9**, 1015 (2018).
[10] W. Legrand, D. Maccariello, F. Ajejas, S. Collin, A. Vecchiola, K. Bouzehouane, N. Reyren, V. Cross, and A. Fert, Nat. Mater. **19**, 34 (2019).
[11] C. Moreau-Luchaire, C. Moutafis, N. Reyren, J. Sampaio, C. A. F. Vaz, N. Van Horne, K. Bouzehouane, K. Garcia, C. Deranlot, P. Warnicke, P. Wohlhüter, J.-M. George, M. Weigand, J. Raabe, V. Cros, and A. Fert, Nature Nanotechnology **11**, 444 (2016).
[12] O. Boulle, J. Vogel, H. Yang, S. Pizzini, D. de Souza Chaves, A. Locatelli, T. O. Menteş, A. Sala, L. D. Buda-Prejbeanu, O. Klein, *et al.*, Nat.

Nanotechnol. **11**, 449 (2016).
[13] A. Soumyanarayanan, M. Raju, A. G. Oyarce, A. K. Tan, M.-Y. Im, A. Petrović, P. Ho, K. Khoo, M. Tran, C. Gan, *et al.*, Nat. Mater. **16**, 898 (2017).
[14] I. Dzyaloshinsky, Journal of Physics and Chemistry of Solids **4**, 241 (1958).
[15] T. Moriya, Phys. Rev. **120**, 91 (1960).
[16] A. Liechtenstein, M. Katsnelson, V. Antropov, and V. Gubanov, Journal of Magnetism and Magnetic Materials **67**, 65 (1987).
[17] B. Göbel, I. Mertig, and O. A. Tretiakov, Phys. Rep. 10.1016/j.physrep.2020.10.001 (2020).
[18] A. Belabbes, G. Bihlmayer, F. Bechstedt, S. Blügel, and A. Manchon, Phys. Rev. Lett. **117**, 247202 (2016).
[19] A. Fert, N. Reyren, and V. Cross, Nat. Rev. Mater. **2**, 17031 (2017).
[20] S. Bornemann, O. Šipr, S. Mankovsky, S. Polesya, J. B. Staunton, W. Wurth, H. Ebert, and J. Minár, Phys. Rev. B **86**, 104436 (2012).
[21] M. Finazzi, M. Savoini, A. Khorsand, A. Tsukamoto, A. Itoh, L. Duo, A. Kirilyuk, T. Rasing, and M. Ezawa, Phys. Rev. Lett. **110**, 177205 (2013).
[22] S. Komineas and N. Papanicolaou, Phys. Rev. B **92**, 064412 (2015).
[23] H. Vigo-Cotrina and A. Guimarães, J. Magn. Magn. Mater. **507**, 166848 (2020).
[24] S. Zhang, F. Kronast, G. van der Laan, and T. Hesjedal, Nano Lett. **18**, 1057 (2018).
[25] X. Zhang, J. Xia, Y. Zhou, D. Wang, X. Liu, W. Zhao, and M. Ezawa, Phys. Rev. B **94**, 094420 (2016).
[26] J. Zang, M. Mostovoy, J. H. Han, and N. Nagaosa, Phys. Rev. Lett. **107**, 136804 (2011).
[27] I. Purnama, W. Gan, D. Wong, and W. Lew, Sci. Rep. **5**, 1 (2015).
[28] S. Frota-Pessôa, Phys. Rev. B **46**, 14570 (1992).
[29] P. R. Peduto, S. Frota-Pessa, and M. S. Methfessel, Phys. Rev. B **44**, 13283 (1991).
[30] A. B. Klautau, S. B. Legoas, R. B. Muniz, and S. Frota-Pessôa, Phys. Rev. B **60**, 3421 (1999).
[31] D. C. M. Rodrigues, A. Szilva, A. B. Klautau, A. Bergman, O. Eriksson, and C. Etz, Phys. Rev. B **94**, 014413 (2016).
[32] M. M. Bezerra-Neto, M. S. Ribeiro, B. Sanyal, A. Bergman, R. B. Muniz, O. Eriksson, and A. B. Klautau, Scientific Reports **3**, 3054 (2013).
[33] R. Cardias, M. M. Bezerra-Neto, M. S. Ribeiro, A. Bergman, A. Szilva, O. Eriksson, and A. B. Klautau, Phys. Rev. B **93**, 014438 (2016).
[34] Y. O. Kvashnin, R. Cardias, A. Szilva, I. Di Marco, M. I. Katsnelson, A. I. Lichtenstein, L. Nordström, A. B. Klautau, and O. Eriksson, Phys. Rev. Lett. **116**, 217202 (2016).
[35] A. B. Klautau and S. Frota-Pessôa, Phys. Rev. B **70**, 193407 (2004).
[36] A. Bergman, L. Nordström, A. B. Klautau, S. Frota-Pessôa, and O. Eriksson, Surface Science **600**, 4838 (2006).
[37] S. Frota-Pessôa, A. B. Klautau, and S. B. Legoas, Phys. Rev. B **66**, 132416 (2002).
[38] R. Haydock, Computer Physics Communications **20**, 11 (1980).
[39] N. Beer and D. G. Pettifor, The recursion method and the estimation of local densities of states, in *The Electronic Structure of Complex Systems* (Springer US, 1984).
[40] U. von Barth and L. Hedin, Journal of Physics C Solid State Physics **5**, 1629 (1972).
[41] S. Frota-Pessôa, R. B. Muniz, and J. Kudrnovský, Phys. Rev. B **62**, 5293 (2000).
[42] R. Cardias, A. Bergman, A. Szilva, Y. O. Kvashnin, J. Fransson, A. B. Klautau, O. Eriksson, and L. Nordström, Scientific Reports **10**, 20339 (2020).
[43] V. P. Antropov, M. I. Katsnelson, B. N. Harmon, M. van Schilfgaarde, and D. Kusnezov, Phys. Rev. B **54**, 1019 (1996).
[44] O. Eriksson, A. Bergman, L. Bergqvist, and J. Hellsvik, *Atomistic Spin Dynamics: Foundations and Applications* (Oxford University Press, Oxford, 2017) p. 272.
[45] B. Skubic, J. Hellsvik, L. Nordström, and O. Eriksson, Journal of Physics: Condensed Matter **20**, 315203 (2008).
[46] T. L. Gilbert, Phys. Rev. **100**, 1243 (1955).
[47] E. Barati, M. Cinal, D. Edwards, and A. Umerski, Phys. Rev. B **90**, 014420 (2014).
[48] S. Mizukami, X. Zhang, T. Kubota, H. Naganuma, M. Oogane, Y. Ando, and T. Miyazaki, Appl. Phys. Express **4**, 013005 (2011).
[49] L. Bergqvist, A. Taroni, A. Bergman, C. Etz, and O. Eriksson, Phys. Rev. B **87**, 144401 (2013).
[50] S. Frota-Pessôa, R. B. Muniz, and J. Kudrnovský, Phys. Rev. B **62**, 5293 (2000).
[51] A. Crépieux and C. Lacroix, Journal of Magnetism and Magnetic Materials **182**, 341 (1998).
[52] G. J. Vida, E. Simon, L. Rózsa, K. Palotás, and L. Szunyogh, Phys. Rev. B **94**, 214422 (2016).
[53] D. Iaia, A. Kubetzka, K. von Bergmann, and R. Wiesendanger, Phys. Rev. B **93**, 134409 (2016).
[54] S. von Malottki, P. F. Bessarab, S. Haldar, A. Delin, and S. Heinze, Phys. Rev. B **99**, 060409 (2019).
[55] J. Iwasaki, M. Mochizuki, and N. Nagaosa, Nature communications **4**, 1 (2013).
[56] A. Thiele, Phys. Rev. Lett. **30**, 230 (1973).
[57] J. Sampaio, V. Cros, S. Rohart, A. Thiaville, and A. Fert, Nat. Nanotechn. **8**, 839 (2013).
[58] C. Deger, I. Yavuz, and F. Yildiz, Scientific reports **9**, 1 (2019).
[59] F. Büttner, I. Lemesh, and G. S. Beach, Scientific reports **8**, 1 (2018).
[60] M. Shen, Y. Zhang, J. Ou-Yang, X. Yang, and L. You, Appl. Phys. Lett. **112**, 062403 (2018).
[61] R. Tomasello, E. Martinez, R. Zivieri, L. Torres, M. Carpentieri, and G. Finocchio, Sci. Rep. **4**, 1 (2014).
[62] J. Xia, X. Zhang, M. Ezawa, O. A. Tretiakov, Z. Hou, W. Wang, G. Zhao, X. Liu, H. T. Diep, and Y. Zhou, Appl. Phys. Lett. **117**, 012403 (2020).
[63] B. Zimmermann, G. Bihlmayer, M. Böttcher, M. Bouhassoune, S. Lounis, J. Sinova, S. Heinze, S. Blügel, and B. Dupé, Phys. Rev. B **99**, 214426 (2019).
[64] E. Simon, K. Palotás, L. Rózsa, L. Udvardi, and L. Szunyogh, Phys. Rev. B **90**, 094410 (2014).
[65] L. Rózsa, E. Simon, K. Palotás, L. Udvardi, and L. Szunyogh, Phys. Rev. B **93**, 024417 (2016).
[66] G. Yin, Y. Li, L. Kong, R. K. Lake, C.-L. Chien, and J. Zang, Phys. Rev. B **93**, 174403 (2016).
[67] J. Hagemeister, N. Romming, K. Von Bergmann, E. Vedmedenko, and R. Wiesendanger, Nat. Commun. **6**, 1 (2015).
[68] J. Wild, T. N. Meier, S. Pöllath, M. Kronseder, A. Bauer, A. Chacon, M. Halder, M. Schowalter, A. Rosenauer, J. Zweck, *et al.*, Sci. Adv. **3**, e1701704 (2017).

[69] A. D. Verga, Phys. Rev. B **90**, 174428 (2014).